

Measurement of the total cross section of uranium-uranium collisions at $\sqrt{s_{NN}} = 192.8$ GeVW. Fischer,* A. J. Baltz, M. Blaskiewicz, D. Gassner, K. A. Drees, Y. Luo, M. Minty, P. Thieberger, and M. Wilinski
Brookhaven National Laboratory, Upton, New York 11973, USA

I. A. Pshenichnov

Institute for Nuclear Research, Russian Academy of Sciences, Moscow, Russia

(Received 12 July 2013; published 23 January 2014)

Heavy ion cross sections totaling several hundred barns have been calculated previously for the Relativistic Heavy Ion Collider (RHIC) and the Large Hadron Collider (LHC). These total cross sections are more than an order of magnitude larger than the geometric ion-ion cross sections primarily due to bound-free pair production (BFPP) and electromagnetic dissociation (EMD). Apart from a general interest in verifying the calculations experimentally, an accurate prediction of the losses created in the heavy ion collisions is of practical interest for the LHC, where some collision products are lost in cryogenically cooled magnets and have the potential to quench these magnets. In the 2012 RHIC run uranium ions collided with each other at $\sqrt{s_{NN}} = 192.8$ GeV with nearly all beam losses due to collisions. This allows for the measurement of the total cross section, which agrees with the calculated cross section within the experimental error.

DOI: [10.1103/PhysRevC.89.014906](https://doi.org/10.1103/PhysRevC.89.014906)

PACS number(s): 25.75.Dw, 29.20.db

I. INTRODUCTION

The collisions of relativistic heavy ions have total cross sections as large as hundreds of barns, primarily due to bound-free pair production (BFPP) and electromagnetic dissociation (EMD). These cross sections have been previously calculated for the Relativistic Heavy Ion Collider (RHIC) [1,2] and the Large Hadron Collider (LHC) [3,4].

Secondary beams created by BFPP can limit the LHC heavy ion luminosity since they have a different charge-to-mass ratio than the primary beam and can be lost in cryogenically cooled magnets. The heat generated due to this loss can quench these magnets when exceeding a threshold. Localized beam losses of a secondary beam generated by BFPP were observed in RHIC with Cu + Cu collisions [5]. The secondary beams generated in Au + Au and U + U collisions in RHIC are within the transverse momentum aperture but outside the longitudinal acceptance of the radio frequency (rf) buckets. These secondary beams are eventually lost, but not in the same turn.

In 2012 RHIC operated for the first time with uranium ions, which have a prolate shape. Such collisions are interesting for several reasons. Collisions of uranium ions along their long axis can potentially create a quark-gluon plasma even denser than that from collisions of the more spherical gold ions. Central collisions of uranium ions with the long axes parallel create elliptic flow [6] of secondary particles, but without the magnetic field generated by the ions passing each other when the elliptic flow is generated through partial overlap of the ions.

In uranium-uranium operation [7] with a low-loss magnetic lattice [8] and three-dimensional stochastic cooling in store [9–11], the beam loss of a well-tuned machine can be almost entirely attributed to luminous processes. In this situation the

total cross section can be obtained from the observed beam loss rates.

In the following we present the calculations for the total U + U cross section for the RHIC operating energy, the main features of the U + U operation during 2012, the methodology for determining the total cross section experimentally, and the experimental result.

II. CALCULATED TOTAL CROSS SECTION

The calculated U + U cross sections at RHIC are shown in Table I together with the RHIC Au + Au and LHC Pb + Pb cross sections. The largest contributions to these cross sections come not from the nuclear overlap of the colliding ions but from two electromagnetic processes, bound-electron free-positron pair (BFPP) production and electromagnetic dissociation (EMD) of the nucleus. Bound-electron free-positron pair production changes the charge of the ion, causing it to fall out of the beam. Electromagnetic dissociation removes at least one neutron from the ion, changing its mass and likewise causing it to fall out of the beam.

Since the total U + U cross section measured here is obtained from beam loss rates, processes that do not lead to beam loss are obviously not included in the calculated cross sections. At RHIC energies the infinite-range elastic Coulomb scattering cross section does not cause any notable deviation in the beam trajectories. The U + U cross section for free electron positron pairs in this experiment is huge, 64 kb calculated with the perturbative formula of Racah [12] (a formula which agrees very well with recent numerical calculations and is much more accurate than the formula of Landau and Lifschitz [13]). For Au + Au at RHIC the corresponding perturbative cross section is 36 kb. However, these free pair cross sections are almost completely dominated by soft pairs, where the ions remain intact, and they do not contribute to the present measured total cross section.

*Wolfram.Fischer@bnl.gov

TABLE I. Calculated total cross sections for Au + Au and U + U collisions in RHIC and Pb + Pb collisions in the LHC. The total cross section is given by the sum of BFPP, single EMD, and nuclear cross sections. The mutual EMD cross section is given for reference only.

Collider Species		RHIC	RHIC	LHC
$\sqrt{s_{NN}}$	GeV	Au + Au	U + U	Pb + Pb
		200	192.8	5520
BFPP	b	117	329	272
Single EMD	b	94.15	150.1	215
<i>Mutual EMD</i>	b	3.79	7.59	6.2
Nuclear	b	7.31	8.2	7.9
Total	b	218.46	487.3	494.9

A. Bound-free pair production (BFPP)

The calculated BFPP cross section for the process

$$^{238}\text{U}^{92+} + ^{238}\text{U}^{92+} \rightarrow ^{238}\text{U}^{92+} + ^{238}\text{U}^{91+} + e^+ \quad (1)$$

is listed in Table I. They are derived from the paper of Meier *et al.* [14]. In this work exact Dirac wave functions are used for final-state bound electrons, and higher shell states are included. Exact Coulomb distorted Dirac wave functions are also used for the final-state continuum positrons. Calculations are perturbative, and semiclassical straight line trajectories are assumed for the ions. However, higher order effects should be small: Exact calculations have been done in the ultrarelativistic limit for RHIC Au + Au, and they show a modest reduction on the order of 3% from perturbation theory in the BFPP cross section to the dominant lowest electron bound $1s$ state [15].

The cross sections calculated in Ref. [14] are compared in that paper with other calculations in the literature and found to be in good agreement. Because of the thoroughness and the convenient presentation of the results in a useful form, we consider those results [14] the current state of the art for BFPP calculations.

B. Electromagnetic dissociation (EMD)

Ultrapерipheral collisions of uranium nuclei at RHIC are characterized by the range of the impact parameter $b > 2R_U$, where R_U is the radius of uranium nucleus. It is measured along the major axis of a prolate uranium nucleus spheroid. The thickness of the diffuse nuclear boundary is included in R_U to avoid any overlap of nuclear densities at $b > 2R_U$. In any case, we are ultimately interested in the sum of electromagnetic dissociation and dissociation from hadronic collisions of the nuclei as discussed below in Sec. II C. There is a smooth transition as a function of decreasing impact parameter from electromagnetic to hadronic dissociation, and the total dissociation will be relatively insensitive to variations of R_U . This insensitivity with variations in R was shown in an early calculation of the Au + Au RHIC case [16].

Strong nuclear forces are not involved in electromagnetic dissociation, but nuclei can be disintegrated by the impact of Lorentz-contracted Coulomb fields of the collision partners. This phenomenon is well known as electromagnetic dissociation (EMD) of nuclei; see, e.g., Refs. [17,18] and references therein. EMD events are classified into single and

mutual dissociation events since experiments at heavy ion colliders make it possible to register dissociation of nuclei either from one beam (with their collision partners frequently left intact) or simultaneously from both beams. This is contrary to collisions with strong interaction, which typically lead to mutual fragmentation of the colliding nuclei.

The single EMD cross section is a part of the total cross section measured in this work, while the mutual EMD cross section is relevant to luminosity measurements performed via the detection of correlated neutron emission in the Zero Degree Calorimeters (ZDC), see Appendix C for details.

EMD cross sections for beam nuclei can be reliably calculated using the Weizsäcker-Williams method of equivalent photons with measured total photoabsorption cross sections for these nuclei used as input. As demonstrated recently [19,20], the RELDIS model [18,21] describes well the absolute cross sections of neutron emission in single and mutual dissociation events resulting from ultraperipheral collisions of lead nuclei at the LHC. RELDIS is based on the Weizsäcker-Williams method of equivalent photons and simulates their absorption by nuclei by means of the Monte Carlo method.

In most events an excited heavy nuclear residue is created, which then evaporates neutrons. As predicted by RELDIS, only 3% of single EMD events of lead nuclei at the LHC are without neutron emission. Therefore, the neutron emission EMD cross section for heavy nuclei serves as a good approximation of the total EMD cross section, but they are still distinguishable. For U + U collision in RHIC the most common event is the single EMD process

$$^{238}\text{U}^{92+} + ^{238}\text{U}^{92+} \rightarrow ^{238}\text{U}^{92+} + ^{237}\text{U}^{92+} + n. \quad (2)$$

The total single and mutual EMD cross sections calculated with RELDIS for Au + Au and U + U collisions in RHIC and Pb + Pb collisions at the LHC are listed in Table I. A Z^2 factor—the square of the charge of the colliding nuclei—increases the total EMD cross sections in U + U collisions compared to Au + Au collisions. This factor controls the intensity of the equivalent photon flux. In particular, as this factor appears twice in calculations of the mutual EMD cross section, the cross section calculated for U + U collisions at RHIC is twice as large as for Au + Au collisions with the same $\sqrt{s_{NN}}$. The mutual EMD cross section calculated for U + U collisions approaches the total nuclear cross section for such heavy and highly charged ion species. According to the RELDIS model, in addition to neutron emission, approximately 60% of electromagnetic excitation events of uranium nuclei lead to their fission.

C. Hadronic collisions of nuclei

It is common to calculate the total cross section of hadronic collisions of nuclei (with overlap of their nuclear densities) by means of the Glauber model [22], which usually gives the total geometrical collision cross section. A similar approach is calculating the total reaction cross sections for collisions of Pb nuclei with various targets in the abrasion-ablation model [23], which we also employ in the present work for calculating total cross sections.

In addition to the distributions of nuclear densities of colliding nuclei, the elementary nucleon-nucleon cross section is a key input in Glauber-type calculations. Even soft fragmentation (e.g., a knock out of one or two nucleons) leads to beam loss in a collider. Therefore, we use the total nucleon-nucleon collision cross section in our calculations instead of the inelastic one. We set the total nucleon-nucleon cross section to 52 and 95 mb for collisions at RHIC and LHC, respectively, according to the compilation from Ref. [24]. This gives us the cross section for Au + Au at $\sqrt{s_{NN}} = 200$ GeV of 7.31 b, in full agreement with the total geometrical cross section in the optical limit, 7.28 b, from Ref. [22]. The calculated total nuclear cross sections are also shown in Table I.

III. RHIC IN U + U OPERATION

The Relativistic Heavy Ion Collider (RHIC) [25,26] consists of two independent rings of 3.8 km circumference, named Blue and Yellow. It has 6 interaction points (IPs) and presently provides collisions for two experiments, STAR at IP6 and PHENIX at IP8. Since 2000 RHIC has collided U + U, Au + Au, Cu + Au, Cu + Cu, $d + Au$, and polarized protons at 15 different energies. Recent upgrades have increased the heavy ion luminosity by an order of magnitude through bunched beam stochastic cooling during stores [9–11].

In 2012 uranium ions were collided for the first time in RHIC, which was also the first time for any hadron collider [7]. This was possible because a new electron beam ion source (EBIS) [27] was recently commissioned that could provide enough intensity for collider operation. The magnetic lattice was selected to provide a large dynamic aperture for on- and off-momentum particles with a beam envelope function β^* at the IP slightly larger than in previous years [8]. Table II shows the main beam parameters typical for the highest luminosity stores at the end of the 2012 running period. A total of 60 stores were provided for the experiments, with an average store length of 6.4 h.

TABLE II. Main beam parameters during U + U operation. Values given are typical for the highest luminosity stores at the end of the 2012 running period. The initial value is at the beginning of stores; the value at \mathcal{L}_{\max} is when the luminosity reached its maximum during the store, typically 1 h after the store started.

Parameter	Unit	Value	
		Initial	At \mathcal{L}_{\max}
Beam energy E	GeV/nucleon	96.4	
Number of bunches n		111	
Bunches colliding at IP6 n_{c6}		102	
Bunches colliding at IP8 n_{c8}		111	
Bunch intensity N_b	10^9	0.3	0.27
Average beam current I_b	mA	38	34
Normalized rms emittance ε_{xy}	μm	2.25	0.40
Luminosity \mathcal{L}/IP	$10^{26} \text{ cm}^{-2} \text{ s}^{-1}$	3	9
Absolute beam loss rate \dot{N}	1000/s	350	900
Relative beam loss rate \dot{N}/N	%/h	4	10

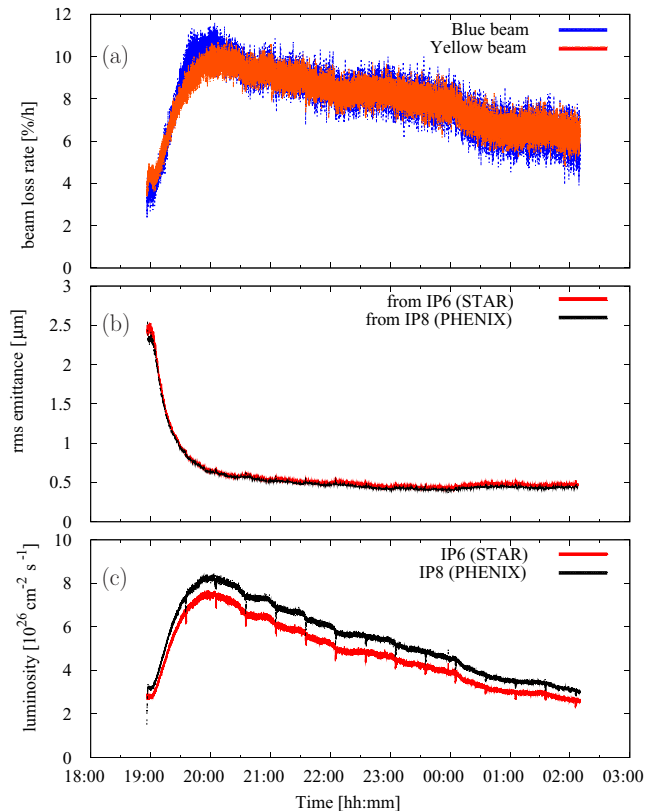


FIG. 1. (Color online) U + U store (fill number 16858) with relative beam loss rates (a), normalized rms emittances calculated from luminosity and intensity (b), and luminosities at the STAR and PHENIX experiments (c). The reduction in the emittances and the corresponding increase in the luminosity are due to stochastic cooling during store.

The year 2012 was also the first in which full three-dimensional stochastic cooling (i.e., horizontal, vertical, and longitudinal) was available in both rings. For uranium beams the cooling was so strong that the transverse emittances were reduced by a factor of four (Fig. 1). The emittances are constant once the transverse intrabeam scattering growth rates [28] and the cooling rates are in equilibrium. The peak luminosity increased by a factor of three (Fig. 1), and the average store luminosity increased by a factor of five.

The 111 bunches leave 10% of the circumference empty to allow for the abort kicker field strength to rise before arrival of the first bunch. With this abort gap, all 111 bunches collided in the PHENIX experiment, but only 102 bunches collided in the STAR experiment. This accounts for the visible difference in the STAR and PHENIX luminosities.

The emittance shown in Fig. 1 is averaged over all four transverse planes of both beams and is calculated from the collision rate and the intensities. The low-loss lattice and the cooling resulted in beam losses (also visible in Fig. 1) nearly exclusively from burnoff through collisions. We discuss this in detail below.

IV. TOTAL CROSS SECTION MEASUREMENT

For round beams of the same size in both rings the time-dependent luminosity is given by [29,30]

$$\mathcal{L}(t) = (\beta\gamma) \frac{n_c}{T_{\text{rev}}} \frac{N_{bB} N_{bY}}{4\pi\epsilon\beta^*} h(\sigma_s, \beta^*), \quad (3)$$

where γ is the Lorentz factor, and $\gamma^2 = 1/(1 - \beta^2)$, n_c is the number of colliding bunches ($n_{c6} = 102$ for \mathcal{L}_6 at STAR, $n_{c8} = 111$ for \mathcal{L}_8 at PHENIX), T_{rev} is the revolution time, N_{bB}, N_{bY} are the Blue and Yellow bunch intensities, $\epsilon = \epsilon_{x,B} = \epsilon_{y,B} = \epsilon_{x,Y} = \epsilon_{y,Y}$ is the normalized rms emittance, and $\beta^* = \beta_{x,B}^* = \beta_{y,B}^* = \beta_{x,Y}^* = \beta_{y,Y}^* = \beta_{y,Y}^*$ is the beam envelope function at the IP. The factor $h(\sigma_s, \beta^*)$, σ_s being the longitudinal rms beam size, is not larger than and is of order 1. It captures the hourglass and crossing angle effect. For Gaussian longitudinal distributions h can be calculated [29]. In the case of RHIC a numerical integration over the measured longitudinal particle distributions is necessary since the beams are held in two radio frequency systems (harmonic numbers $h = 360$ and $h = 7 \times 360$) and the bunches span several of the higher harmonic buckets at the end of a store.

In the case where all beam losses are given by the total U + U cross section σ_{tot} we have

$$\frac{dN_B(t)}{dt} = \frac{dN_Y(t)}{dt} = -[\mathcal{L}_6(t) + \mathcal{L}_8(t)] \sigma_{\text{tot}}, \quad (4)$$

where N_B and N_Y are the Blue and Yellow beam total intensities and $\mathcal{L}_6(t)$ and $\mathcal{L}_8(t)$ are the instantaneous luminosities at IP6 (STAR) and IP8 (PHENIX) respectively. The total cross section is then given by

$$\sigma_{\text{tot}} = -\frac{\dot{N}_{B,Y}(t)}{[\mathcal{L}_6(t) + \mathcal{L}_8(t)]} \quad (5)$$

and the systematic relative error is given by

$$\frac{\Delta\sigma^{\text{sys}}}{\sigma_{\text{tot}}} = \frac{\Delta\dot{N}_{B,Y}^{\text{sys}}}{\dot{N}_{B,Y}} + \frac{\Delta\mathcal{L}_6^{\text{sys}} + \Delta\mathcal{L}_8^{\text{sys}}}{\mathcal{L}_6 + \mathcal{L}_8}, \quad (6)$$

where $\Delta\dot{N}_{B,Y}^{\text{sys}}$ and $\Delta\mathcal{L}_{6,8}^{\text{sys}}$ are the systematic errors of the beam loss rate and luminosity, respectively. If timing errors can be neglected (see Sec. IV C) we can use

$$\frac{\Delta\dot{N}_{B,Y}^{\text{sys}}}{\dot{N}_{B,Y}} = \frac{\Delta N_{B,Y}^{\text{sys}}}{N_{B,Y}} \quad (7)$$

and the systematic error becomes

$$\Delta\sigma^{\text{sys}} = \sigma_{\text{tot}} \left(\frac{\Delta N_{B,Y}^{\text{sys}}}{N_{B,Y}} + \frac{\Delta\mathcal{L}_6^{\text{sys}} + \Delta\mathcal{L}_8^{\text{sys}}}{\mathcal{L}_6 + \mathcal{L}_8} \right). \quad (8)$$

We also note that if all beam losses are due to burnoff, both the transverse and longitudinal emittances are constant, and all bunches collide at IP6 and IP8 (i.e., $n_{c6} = n_{c8} = n_c$), the intensities and luminosities can be written as

$$N_{B,Y}(t) = \frac{N_{B,Y}(0)}{1 + t/\tau} \quad \text{and} \quad \mathcal{L}_{6,8}(t) = \frac{\mathcal{L}_{6,8}(0)}{(1 + t/\tau)^2}, \quad (9)$$

where the time constant τ follows from Eq. (4) as

$$\tau = \frac{N_{B,Y}(0)}{[\mathcal{L}_6(0) + \mathcal{L}_8(0)] \sigma_{\text{tot}}}. \quad (10)$$

We need to obtain the beam loss rates $\dot{N}_{B,Y}$ and the luminosities $\mathcal{L}_{6,8}$ for the determination of the total cross section σ_{tot} via Eq. (5). The beam loss rate is calculated from a time-dependent measurement of the total beam intensity with a parametric current transformer (PCT, Appendix B). The total intensity is reported every second and the loss rate is calculated as the slope over an interval of 20 s. The luminosity is measured via the detection of neutron pairs in time coincidence in the zero degree calorimeter (ZDC) [31] (Appendix C). The luminosity is also reported every second.

A. Luminous and nonluminous losses

A principal limitation of the method used here comes from the fact that there can be beam losses from other processes than U + U interactions given by the total cross section σ_{tot} . In a situation with nonluminous losses, the use of Eq. (5) will give only an upper limit for σ_{tot} if these nonluminous losses are not subtracted.

A number of tests are available to assess if there are nonluminous losses:

- (1) The Blue and Yellow beam loss rates $\dot{N}_{B,Y}$ must be the same if all losses are luminous.
- (2) The Blue and Yellow beam loss rates $\dot{N}_{B,Y}$ must be proportional to the total luminosity $\mathcal{L}_6 + \mathcal{L}_8$.
- (3) The beam loss rates $\dot{N}_{B,Y}$ must be zero for noncolliding beams.

These are necessary but not sufficient conditions for all beam losses to be luminous. We use conditions 1 and 2 later to guide the data selection but we have no direct experimental data to test condition 3.

There are a number of processes that can lead to nonluminous beam losses:

- (1) Intrabeam scattering
- (2) Residual gas elastic scattering
- (3) Dynamic aperture and beam-beam effects
- (4) Residual gas inelastic scattering

In our discussion we need to separate emittance growth processes from beam loss processes. Emittance growth will eventually lead to beam loss once a limiting aperture is reached by the particles with the largest amplitudes. With stochastic cooling, the emittance growth is reversed and an equilibrium emittance is reached for processes with growth times comparable to or smaller than the cooling time of about 1 h. Items 1–3 of the above list fall in this category.

In some processes the particle amplitudes can be increased much faster than the cooling time. Item 3 can and item 4 does fall in this category. These processes are discussed in detail in Appendix A and summarized in Table III. We must expect that there are a small number of particles lost through processes other than burnoff, and our analysis of the experimental data needs to take this into account. The predominant process is inelastic scattering on the residual gas, leading to beam loss rates which are about 10% of the total loss rate at the beginning of the store, and 3% at the time of \mathcal{L}_{max} (see Table III and Fig. 2).

TABLE III. Emittance growth and nonluminous beam loss for U + U collisions in RHIC with beam parameters given in Table II. Formulas are given in Appendix A. The values are shown for either the beginning of store or the time of \mathcal{L}_{\max} , whichever gives the larger emittance growth or beam loss. The emittance growth times are calculated in the absence of cooling; cooling times are of order 1 h. Only the warm regions of the vacuum system are considered in the calculation of residual gas effects. The cold regions with cryopumping have very low particle densities.

Parameter	Unit	Value
<i>Warm vacuum sections</i>		
Length per ring l_w	m	652
Gas temperature	K	300
Average pressure $\langle P \rangle$	nTorr	0.5
Static gas composition		95% H ₂ , 5% CO
Average β functions $\langle \beta \rangle$	m	115
<i>Emittance growth from intrabeam scattering</i>		
Transverse emittance growth time τ_{ϵ_n}	h	0.44
Longitudinal emittance growth time τ_{ϵ_s}	h	0.55
<i>Transverse emittance growth from residual gas elastic scattering</i>		
Emittance growth coefficient for N ₂	s ⁻¹ Torr ⁻¹	0.88
N ₂ equivalent pressure	nTorr	0.5
Emittance growth time τ_{ϵ_n} , at \mathcal{L}_{\max}	h	49
<i>Beam loss from residual gas inelastic scattering</i>		
Coefficient for beam loss on N ₂	s ⁻¹ Torr ⁻¹	800
N ₂ equivalent pressure	nTorr	0.1
Beam lifetime $\tau_N = N_{B,Y}/\dot{N}_{B,Y}$	h	498
Loss rate $\dot{N}_{B,Y}$, initial	1000 s ⁻¹	19

B. Measurement value and statistical error

There were 60 physics U + U stores with an average length of 6.4 h (Table IV). As a first step we selected all stores

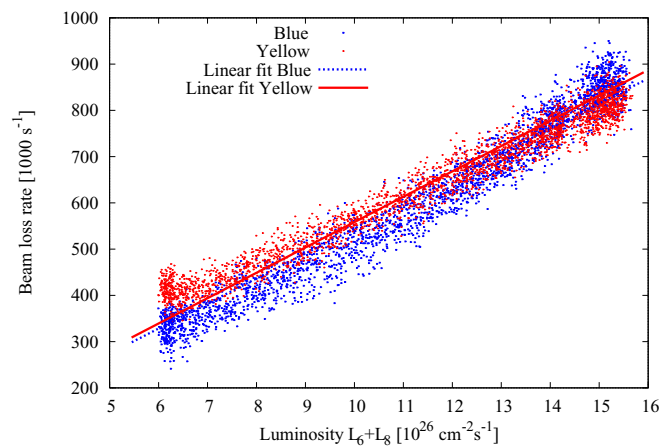


FIG. 2. (Color online) Blue and Yellow beam loss rates as a function of the total luminosity $\mathcal{L}_6 + \mathcal{L}_8$ for fill number 16858. The units for the luminosity and beam loss rates are chosen so that the linear fit coefficient is returned in units of barn. Fitted values for this case are $\sigma_{\text{tot}} = (516.53 \pm 0.21)$ b for Blue, and $\sigma_{\text{tot}} = (549.61 \pm 0.16)$ b for Yellow. The error is the statistical standard error.

TABLE IV. U + U store overview for σ_{tot} determination.

Parameter	Unit	Value
No. of physics stores		60
Average store length	h	6.4
No. of stores selected with \dot{N}_B data		8
No. of stores selected with \dot{N}_Y data		20
Total number of data points (\dot{N}, \mathcal{L})		554 k

which did not have any unusually high beam losses, and in which the Blue and Yellow beam loss rates \dot{N}_B and \dot{N}_Y were approximately equal and proportional to the total luminosity $\mathcal{L}_6 + \mathcal{L}_8$ for at least a period of the store. These were the last 50 of all 60 physics stores.

For each of these stores a fitted value for σ_{tot} was obtained by assuming that all losses are luminous, i.e., by fitting a straight line to all pairs (\dot{N}, \mathcal{L}) imposing the condition of a zero offset. The fits for one store are shown in Fig. 2, and the caption notes the standard statistical error for the fit.

Figure 3 shows the so-fitted σ_{tot} values for all preselected stores. The earlier stores (fill numbers 16796 to 16817) show a much larger fitted σ_{tot} value than the later stores, indicating that not all beam losses were luminous. We note that all preselected stores have longitudinal stochastic cooling and that transverse stochastic cooling became available in the Yellow ring beginning with fill number 16816 and in the Blue ring with fill number 16820, initially in the vertical plane only. Beginning with fill number 16832 in the Yellow ring and 16835 in the Blue ring, the beams were cooled in all three dimensions. We further restrict our data selections to fill number 16820 and larger. But even for those fills we cannot be sure that all losses are luminous. Indications of this are the differences in the

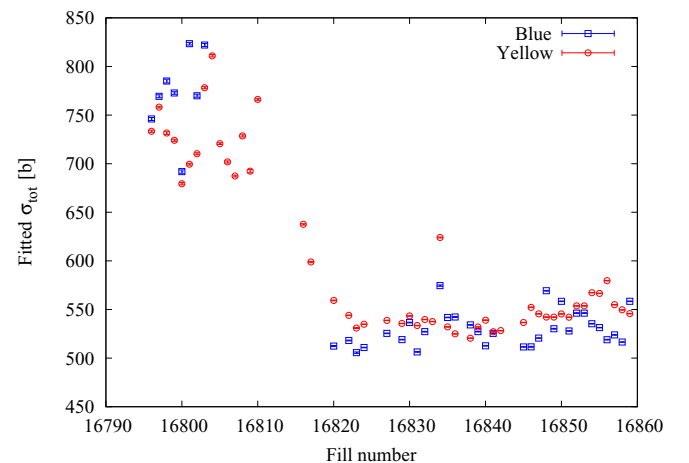


FIG. 3. (Color online) Fitted σ_{tot} for all (partial) stores during which the beam loss rate was proportional to the total luminosity $\mathcal{L}_6 + \mathcal{L}_8$. All fills shown have longitudinal cooling. Vertical cooling started in Yellow with fill 16816 and in Blue with fill 16820. Horizontal cooling started in Yellow with fill 16832 and in Blue with fill 16835. In fill 16834 a cavity tripped, leading to an increase in the momentum spread.

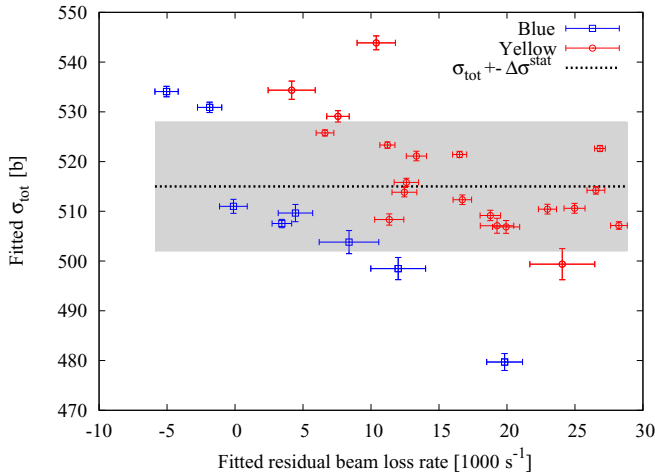


FIG. 4. (Color online) Fitted σ_{tot} and fitted residual beam loss rates for selected stores. The errors of the individual data points are the standard errors from the linear fit. Shown is also the average of the σ_{tot} values and the rms error of the combined individual data points as the gray area, giving $\sigma_{\text{tot}} = (515 \pm 13^{\text{stat}})$ b.

fitted σ_{tot} from the Blue and Yellow beam in the same store and variations across stores.

In a second step we fit σ_{tot} to the (\dot{N}, \mathcal{L}) data points for all stores with fill number 16820 and larger under the assumption that there are residual beam losses, i.e., with a nonzero offset. In Fig. 4 we show the fitted values for both σ_{tot} and the residual beam loss rates, where we restricted the data selection to data points with a residual beam loss rate not larger than 30000 s^{-1} , about 10% of the minimum and 3% of the maximum beam loss rates observed (see Fig. 2), to ensure that the σ_{tot} determination is done with conditions of nearly all beam losses due to burnoff.

Combining the individual data points in Fig. 4 yields the measurement value and statistical error as $\sigma_{\text{tot}} = (515 \pm 13^{\text{stat}})$ b. We have calculated the statistical error simply as the standard deviation of the σ_{tot} distribution since this distribution is much wider than the statistical errors for the individual data points.

C. Measurement systematic error

If timing errors can be neglected, the systematic error is given by Eq. (8). We will now justify this assumption. The RHIC timing system is driven by a 5-MHz ultra-low-noise temperature-controlled crystal oscillator with a relative

TABLE V. Sources and contributions to the systematic errors in the beam intensity $\Delta N_{B,Y}^{\text{sys}}/N_{B,Y}$ (Appendix B).

Source	Error (%)
Temperature variations	0.19
Bunch pattern	0.10
Calibration error	0.15
PCT accuracy and readout drifts	0.30
Output noise	0.01
Total $\Delta N_{B,Y}^{\text{sys}}/N_{B,Y}$ (quadratic addition)	0.40

TABLE VI. Sources and contributions to the systematic errors in the luminosity $\Delta \mathcal{L}^{\text{sys}}/\mathcal{L}$ (Appendix C and Ref. [50]).

Source	Error (%)
Beam displacement	1.0
Crossing angle	2.0
Intensity	2.7
Statistical	1.7
Total $\Delta \mathcal{L}^{\text{sys}}/\mathcal{L}$ (quadratic addition)	3.9

frequency error of $\pm 10^{-9}$ to $\pm 10^{-10}$ per day [32]. However, the timing error of reported 1-Hz signals, such as intensity and luminosity, have a much larger error. The combined systematic, periodic (due to clock beating), and random timing error can reach values of 1 s, but typically does not exceed 0.5 s. Periodic and random errors with a symmetric distribution around a central value will only translate into statistical errors of the fitted total cross section (see Fig. 2), which we have taken into account already.

Using the data shown in Figs. 1 and 2, a systematic timing error of 0.5 s is equivalent to a maximum systematic relative beam loss error of $(\Delta \dot{N}_{B,Y}/N_{B,Y})_{\text{max}}^{\text{sys}} = 3.8 \times 10^{-5}$ and a maximum systematic relative luminosity error of $(\Delta \mathcal{L}_{6,8}/\mathcal{L}_{6,8})_{\text{max}}^{\text{sys}} = 3.3 \times 10^{-5}$. These are much smaller than other systematic errors for the beam loss rate and luminosity respectively (see below), and we therefore neglect timing errors.

The systematic error σ^{sys} is then determined by the systematic errors of the beam intensity and luminosities. These are discussed in detail in Appendixes B and C respectively. The sources and contributions of all components are summarized in Tables V and VI, and, using Eq. (8) we obtain $\sigma^{\text{sys}} = 22$ b.

V. SUMMARY

In U+U stores at $\sqrt{s_{NN}} = 192.8$ GeV with three-dimensional stochastic cooling nearly all beam losses are from burnoff and the total interaction cross section can be obtained from the observed beam loss rates as

$$\sigma_{\text{tot}}^{\text{meas}} = (515 \pm 13^{\text{stat}} \pm 22^{\text{sys}}) \text{ b}, \quad (11)$$

with a combined statistical and systematic measurement error of 26 b or 5.0%. The principal limitation of the measurement method are nonluminous beam losses that are not accounted for. If these exist the measurement only delivers an upper limit for $\sigma_{\text{tot}}^{\text{meas}}$. The calculated total cross section of $\sigma_{\text{tot}}^{\text{calc}} = 487.3$ b is smaller than the measured one by 28 b or 5.4%, a value close to the combined measurement error.

ACKNOWLEDGMENTS

The authors are thankful to J. Bergoz, S. Binello, R. Bruce, W. Christie, T. Hayes, X. He, M. Mapes, A. Marusic, K. Smith, and J. Jowett for discussions and support. Work was supported by Brookhaven Science Associates, LLC, under Contract No. DE-AC02-98CH10886 with the US Department of Energy.

APPENDIX A: NONLUMINOUS BEAM LOSSES

1. Intrabeam scattering

Intrabeam scattering refers to small changes in the momenta of stored particles due to close encounters with other stored particles, leading to emittance growth [33]. In our case intrabeam scattering is counteracted by stochastic cooling, leading to a reduction of the emittance until an equilibrium value is reached.

Table III shows the emittance growth times

$$\tau_\varepsilon = \left(\frac{1}{\varepsilon} \frac{d\varepsilon}{dt} \right)^{-1} \quad (\text{A1})$$

in the absence of cooling for the transverse and longitudinal planes. Consistent with operational experience, full transverse coupling is assumed and therefore the horizontal and vertical growth rates are equal. The calculation is for the time when \mathcal{L}_{\max} is reached and the emittances are close to their minimum value (Fig. 1).

We also estimate the lifetime of uranium beams due to intrabeam scattering in the presence of cooling. The emittance evolution is shown in Fig. 1 where the asymptotic cooling time is about 1 h. The collimator settings correspond to an rms emittance of $80 \mu\text{rad}$, and the simplest model is to assume the emittance distribution follows

$$\frac{\partial w(\varepsilon, t)}{\partial t} = \frac{\partial}{\partial \varepsilon} \left(a\varepsilon w + M\varepsilon \frac{\partial w}{\partial \varepsilon} \right), \quad (\text{A2})$$

where $w(\varepsilon, t)$ is the time-dependent emittance distribution, a is the cooling rate, and M is the diffusion rate. We have $a = 1 \text{ h}^{-1}$ and $\varepsilon_a = M/a = 0.5 \mu\text{rad}$. If we put a collimator (an element that ensures particle removal when a certain amplitude is exceeded) at a location equivalent to an emittance of $\varepsilon_b = 80 \mu\text{rad}$ the beam lifetime will be [33]

$$\tau_N = \frac{\varepsilon_a}{a\varepsilon_b} \exp\left(\frac{\varepsilon_b}{\varepsilon_a}\right) \sim 10^{67} \text{ h}. \quad (\text{A3})$$

Beam losses from intrabeam scattering with cooling can indeed be neglected.

2. Residual gas elastic scattering

We consider only the warm sections of RHIC since the residual gas density in the cold arcs is very low due to cryopumping. The rms emittance growth time due to residual gas elastic scattering is [34,35]

$$\frac{1}{\tau_{\varepsilon_n}} = \frac{Z}{A} \frac{1}{\varepsilon_n} \frac{d\varepsilon_n}{dt} = \frac{(\beta\gamma)}{\varepsilon_n} \times \frac{1}{C} \int_0^C \beta(s) \theta_{rg}^2(s) ds, \quad (\text{A4})$$

where Z and A are the charge and mass number of the stored ion, C is the circumference, and θ_{rg} is the rms scattering angle. For protons, scattering on species with atomic number Z_i and density n_i , the scattering angle is [34]

$$\theta_{rg}^2(s) = \frac{4\pi r_p^2 c}{\beta^3 \gamma^2} n_i Z_i (Z_i + 1) \ln(183 Z_i^{-1/3}), \quad (\text{A5})$$

where r_p is the classical proton radius and c is the speed of light. For molecular nitrogen N_2 at 300 K one has

$$\frac{1}{\tau_{\varepsilon_n}} \approx 0.88 \text{ s}^{-1} \text{ Torr}^{-1} \frac{l_w}{C} \frac{\langle \beta P \rangle}{\varepsilon_n \gamma}. \quad (\text{A6})$$

where l_w is the length of the warm sections. For other residual gas species the N_2 equivalent pressure can be calculated according to Ref. [34] as

$$P_{\text{N}_2\text{equiv}}^{\text{elast}} = \frac{2 \times 10^{-3}}{P} \sum_i P_i \sum_j k_{ij} Z_{ij} (Z_{ij} + 1) \ln(183 Z_{ij}^{-1/3}), \quad (\text{A7})$$

where P_i is the partial pressure of gas molecules i , and k_{ij} is the number of species j in the gas molecule i . Average β functions of the warm sections and calculated emittance growth times are shown in Table III.

3. Residual gas inelastic scattering

Stored beam particles are lost after an inelastic collision with molecules of the residual gas in the beam pipe. The beam loss rate due to residual gas inelastic scattering of ions on molecular nitrogen N_2 at 300 K is [34,36]

$$-\frac{dN_{B,Y}}{dt} \approx 800 \text{ s}^{-1} \text{ Torr}^{-1} A^{2/3} N_{B,Y} \frac{\langle \beta \rangle}{C} \int_0^C P(s) ds, \quad (\text{A8})$$

where $\langle \beta \rangle$ is the average β function, C is the circumference, and $P(s)$ is the s -dependent N_2 pressure. The nitrogen equivalent pressure can be calculated as [34]

$$P_{\text{N}_2\text{equiv}}^{\text{nucl}} = 0.0861 \sum_i P_i \sum_j k_{ij} A_{ij}^{2/3}, \quad (\text{A9})$$

where P_i is the partial pressure of gas molecules i , k_{ij} are the number of species j in the gas molecule i , and A_{ij} is the mass number of species j in molecule i . We consider only the warm beam pipe regions and neglect the cryogenically pumped cold beam pipe regions. The relevant input data and calculated loss rate are shown in Table III. The calculated loss rate is for the beginning of the store and has an error of approximately a factor of 2, primarily due to the uncertainty in the pressure readings. The beam loss rate due to inelastic scattering decreases throughout the store with the decrease of the number of stored particles.

4. Dynamic aperture and beam-beam effects

Orbit, tune, and chromaticity settings are chosen to minimize nonluminous beam losses. However, actual machine conditions are not always reproducible and can drift with time due to, e.g., temperature changes. Beam losses are monitored continuously during stores, and small parameter changes are periodically made to ensure that the machine operates at the minimum achievable loss rates. We disregard time periods with beam loss rates higher than the consistently low values established over a number of stores.

The motion of hadrons stored in a collider ring is well approximated by Hamiltonian mechanics (non-Hamiltonian effects were discussed above). The particle motion in storage

rings can be and typically is chaotic, which leads to emittance growth and possibly particle loss over the storage time [37–40]. In addition to nonlinear elements such as sextupoles, magnetic field errors in the main dipoles and quadrupoles, and the beam-beam interactions, there are parameter modulations that cause or enhance chaotic motion.

Emittance growth effects due to nonlinear elements and parameter modulations are generally smaller than the cooling time and will not lead to any relevant losses (see Sec. A 1). Chaotic particles can also be lost over much smaller time scales than the cooling time [40]. But with cooling particles remain at small amplitudes, far away from the dynamic aperture, and this is much less likely.

APPENDIX B: INTENSITY MEASUREMENT AND SYSTEMATIC INTENSITY ERROR

The instruments to measure the number of ions present in each RHIC ring are two Bergoz parametric current transformers (PCTs) [41]. These devices, often referred to as DC current transformers (DCCTs), are sophisticated refinements of the basic fluxgate magnetometer [42] invented in the 1930s by Vacquier at Gulf Research Laboratories and used in World War II to detect the proximity of submarines. The version now widely used for accelerator beam instrumentation was invented in 1969 by Unser at CERN [43] and further refined by Bergoz [41] and his collaborators. The PCTs measure all ions circulating, bunched and unbunched. The unbunched beam is never more than a few percent of the total intensity, and since it is distributed over the full circumference, its density is very low. It therefore does not contribute measurably to the luminosity.

It is important to note that this is a zero-crossing device in which the fluxes induced by the beam in very high permeability cores is compensated in a closed feedback loop by a current in windings that produce the opposite fluxes. In addition there are other windings that modulate the fluxes, causing the cores to cross from saturation in one direction to saturation in the opposite direction. These transitions are detected by pickup coils and the lack of symmetry (i.e., the presence of odd harmonics) of these signals is used as the error signal to close the feedback loop. The large dynamic range of these instruments (of order 10^7) is mainly due to the fact that the flux in the cores is near zero no matter what the value is of the measured field. This also means that most measurement errors (except for noise) are only weakly intensity dependent.

Rather than using the internal PCT instrument calibration, we use a precise external current source [44] and digitize the output in a high-precision digital volt meter (DVM) [45]. Both of these instruments are calibrated annually.

The PCT calibration software in LabVIEW determines offset and slope values for the DVM readings as function of calibration current for both PCTs. These values are then used to correct the readings and to arrive at values for the number of ions in each ring by taking into account their charge states and their revolution frequency. PCT calibrations are performed before each running period.

One issue investigated before starting the error evaluation was the placement of the coil used to inject the calibration

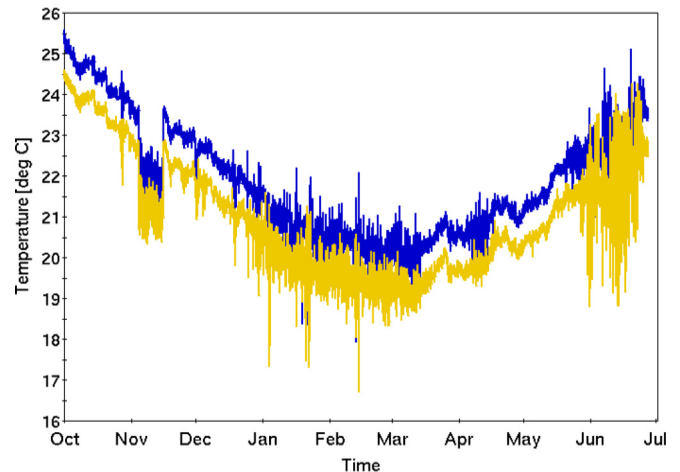


FIG. 5. (Color online) Blue and Yellow ring PCT core temperatures from October 2011 to June 2012, covering the period of the 2012 RHIC run.

current. The concern was that its different geometry compared to the beam may lead to a correction factor that may not have been considered. In fact, some facilities [46] use straight calibration wires parallel to the beam. It was determined that this is not an issue both experimentally and in consultation with experts [47,48]. In the following we discuss one by one the sources of error that contribute to the overall uncertainty in the beam intensity determinations.

1. Temperature variations

According to the PCT user manual, the temperature coefficient for the electronics is $<0.1 \mu\text{A}/\text{K}$ for the electronics but it is typically $5 \mu\text{A}/\text{K}$ for the sensor head. There is no temperature regulation in the system nor are there corrections applied, even though the core temperatures are recorded. Figure 5 shows the temperature of the Blue and Yellow PCTs from October 2011 to July 2012. The maximum variation is 5 K.

Since the PCT calibration used is the one performed just before the 2012 running period when the temperature was highest, and the uranium operation took place from 19 April to 15 May 2012, we use the full 5 K excursion, resulting in a current error due to temperature of $5 \mu\text{A}/\text{K} \times 5 \text{K} = 25 \mu\text{A}$. This translates into an intensity error of 0.19% (Table V).

2. Bunch pattern influence

The variation of the PCT output signal as a function of the bunch pattern, or duty factor, was measured by connecting a variable duty factor DC current supply to the calibration windings (Fig. 6). This measurement shows that the fill pattern contributes less than 0.10% to the systematic intensity error (Table V).

3. Calibration instrument errors

Table VII shows examples for particular ranges for the accuracy in parts per million (ppm) of full scale for the DVM and the current source that are used for the PCT calibrations.

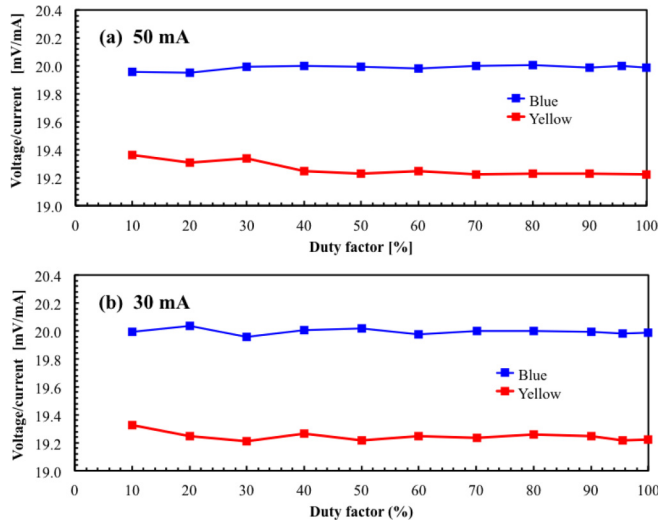


FIG. 6. (Color online) Measurement of the variation of the PCT output signal as a function of duty factor.

We see that the only possibly relevant contribution to the error comes from the current source. It is 0.15% of full scale if we add the drift over one year to the effect of a 5-K temperature uncertainty. This number can be refined to take into account the use of other ranges and of currents that are not full scale. Calibration errors yield an intensity error of 0.15% (Table V).

4. Zero and slope drift

The PCT calibration is typically performed at the beginning of the running period and the question is by how much the calibration parameters can vary during the run. We have already considered the temperature effect above. Here we list other sources of errors that can affect the calibration taken from the specifications found in the PCT user manual:

- (i) Linearity error $\pm 0.01\% \pm$ zero error
- (ii) Zero drift (1 h) $< 1 \mu\text{A}$
- (iii) Zero drift (1 year) $< 5 \mu\text{A}$ at constant temperature
- (iv) Absolute accuracy $> \pm 0.1\%$

We have compared some of these values with slope values for two instances where calibration parameters before and after a calibration were logged and one where calibrations were logged two days apart.

We see that all the slope differences between calibrations are largest for the MADC measurements, which vary by an average of 0.14% when the measurements are months

TABLE VII. Accuracy and temperature coefficients of current calibration instruments [44,45].

Instrument	Range	24 h (ppm)	90 d (ppm)	1 y (ppm)	Temperature coefficient (ppm/K)
Keithley 2000	10 V	15	20	30	2
Keithley 220	100 mA			100,000	10,000

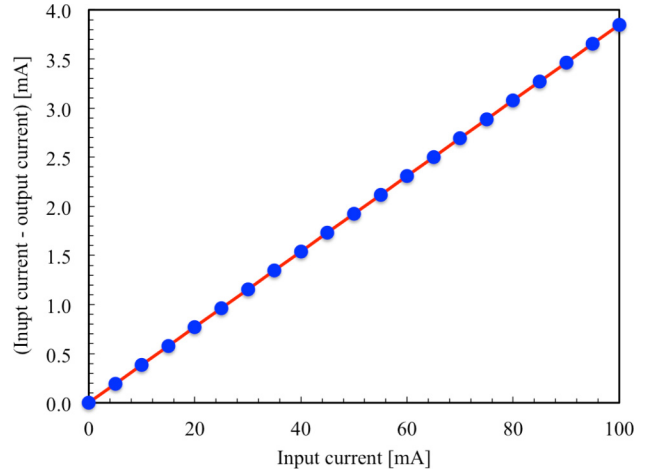


FIG. 7. (Color online) Difference between expected and observed DVM readings. The rms deviation from a straight line is $2.4 \mu\text{A}$, not visible in this plot.

apart and 0.036% when they are two days apart. The DVM measurements are much better than could be expected from the current source specifications. Independent of the digitizer used the slope values always repeat within 0.2%.

5. Noise contributions

In the past, some discrepancies were observed when comparing expected DVM readings with actual readings obtained with a series of current source settings. These discrepancies were attributed to noise. Such measurements were repeated. Figure 7 shows the differences between expected and observed values and the quality of linear least square fit indicates that the discrepancies are mainly due to a calibration issue, which is compensated for in the calibration procedure.

The error sources and values are summarized in Table V. For those errors that were obtained in units of current, such as the temperature correction, the values were converted to percentages by using an average beam current of 28 mA, typical for the uranium beams midstore in the experiments (Table II shows the values at the beginning of the store and at the time of the maximum luminosity). Output noise contributes only 0.01% to the systematic intensity error (Table V).

APPENDIX C: LUMINOSITY MEASUREMENT AND SYSTEMATIC LUMINOSITY ERROR

The luminosity is measured via the detection of neutron-pair coincidences in the zero degree calorimeter (ZDC) [16,31]. The effective cross section for neutron-pair coincidence detection was measured to be $\sigma_{nn} = 15.79$ b for PHENIX and $\sigma_{nn} = 15.84$ b for STAR. These values are in good agreement with the calculated cross sections given in Table I. Indeed, by accounting for the fact that about 97% of the EMD events are accompanied by the emission of at least one neutron at each side, the value of 15.34 b is obtained as $(0.97 \times 0.97 \times 7.59 + 8.2)$ b, providing that forward neutrons are always emitted in nuclear collisions.

A general outline of the error analysis of luminosity measurements is given in Ref. [49], and the detailed analysis of the U + U luminosity error is given in Ref. [50]. The following effects were considered in the determination of the luminosity error: (i) the need for a double Gaussian fit function

for the luminosity as a function of relative beam offset, (ii) the total intensity measurement, (iii) the bunched intensity measurement, (iv) the fill pattern, (v) the relative position measurement error, and (vi) the crossing angle. A summary of the error sources and contributions is provided in Table VI.

-
- [1] H. Gould, Lawrence Berkeley Laboratory Report No. LBL-18593, 1984 (unpublished).
- [2] A. J. Baltz, M. J. Rhoades-Brown, and J. Weneser, *Phys. Rev. E* **54**, 4233 (1996).
- [3] S. R. Klein, *Nucl. Instrum. Methods Phys. Res., Sect. A* **459**, 51 (2001).
- [4] J. M. Jowett, J.-B. Jeanneret, and K. Schindl, in *Proceedings of the Particle Accelerator Conference 2003* (IEEE, Piscataway, New Jersey, 2003), pp. 1682–1684.
- [5] R. Bruce, J. M. Jowett, S. Gilardoni, A. Drees, W. Fischer, S. Tepikian, and S. R. Klein, *Phys. Rev. Lett.* **99**, 144801 (2007).
- [6] K. H. Ackermann *et al.* (STAR Collaboration), *Phys. Rev. Lett.* **86**, 402 (2001).
- [7] Y. Luo, J. Alessi, M. Bai, E. Beebe, J. Beebe-Wang, I. Blackler, M. Blaskiewicz, J. M. Brennan, K. A. Brown, D. Bruno, J. Butler, R. Connolly, T. D’Ottavio, K. A. Drees, A. V. Fedotov, W. Fischer, C. J. Gardner, D. M. Gassner, X. Gu, Y. Hao, M. Harvey, T. Hayes, L. T. Hoff, H. Huang, P. Ingrassia, J. Jamilkowski, N. A. Kling, M. Lafky, J. S. Laster, C. Liu, D. Maffei, Y. Makdisi, M. Mapes, G. J. Marr, A. Marusic, F. Meot, K. Mernick, R. Michnoff, M. Minty, C. Montag, J. Morris, C. Naylor, S. Nemesure, A. I. Pikin, P. Pile, V. Ptitsyn, D. Raparia, G. Robert-Demolaize, T. Roser, P. W. Sampson, J. Sandberg, V. Schoefer, C. Schultheiss, F. Severino, T. Shrey, K. Smith, S. Tepikian, P. Thieberger, D. Trbojevic, J. Tuozzolo, B. Van Kuik, G. Wang, M. Wilinski, A. Zaltsman, K. Zeno, S. Y. Zhang, and W. Zhang, in *Proceedings of the International Particle Accelerator Conference 2013* (JACoW.org, Geneva, 2013), pp. 1538–1540.
- [8] Y. Luo, M. Blaskiewicz, W. Fischer, X. Gu, and S. Tepikian, in *Proceedings of the International Particle Accelerator Conference 2012* (JACoW.org, Geneva, 2012), pp. 175–177.
- [9] M. Blaskiewicz and J. M. Brennan, *Phys. Rev. ST Accel. Beams* **10**, 061001 (2007).
- [10] M. Blaskiewicz, J. M. Brennan, and F. Severino, *Phys. Rev. Lett.* **100**, 174802 (2008).
- [11] M. Blaskiewicz, J. M. Brennan, and K. Mernick, *Phys. Rev. Lett.* **105**, 094801 (2010).
- [12] G. Racah, *Nuovo Cimento* **14**, 93 (1937).
- [13] L. D. Landau and E. M. Lifshitz, *Phys. Z. Sowjetunion* **6**, 244 (1934).
- [14] H. Meier, Z. Halabuka, K. Hencken, D. Trautmann, and G. Baur, *Phys. Rev. A* **63**, 032713 (2001).
- [15] A. J. Baltz, *Phys. Rev. Lett.* **78**, 1231 (1997).
- [16] A. J. Baltz, C. Chasman, and S. N. White, *Nucl. Instrum. Methods A* **417**, 1 (1998).
- [17] A. J. Baltz, G. Baur, D. d’Enterria, L. Frankfurt, F. Gelis, V. Guzey, K. Hencken, Yu. Kharlov, M. Klasen, S. R. Klein, V. Nikulin, J. Nystrand, I. A. Pshenichnov, S. Sadovsky, E. Scapparone, J. Seger, M. Strikman, M. Tverskoy, R. Vogt, and S. N. White, *Phys. Rep.* **458**, 1 (2008).
- [18] I. A. Pshenichnov, *Phys. Part. Nuclei* **42**, 215 (2011).
- [19] C. Oppedisano, *J. Phys. G* **38**, 124174 (2011).
- [20] B. Abelev *et al.* (ALICE Collaboration), *Phys. Rev. Lett.* **109**, 252302 (2012).
- [21] I. A. Pshenichnov, J. P. Bondorf, I. N. Mishustin, A. Ventura, and S. Masetti, *Phys. Rev. C* **64**, 024903 (2001).
- [22] M. L. Miller, K. Reygers, S. J. Sanders, and P. Steinberg, *Ann. Rev. Nucl. Part. Sci.* **57**, 205 (2007).
- [23] C. Scheidenberger, I. A. Pshenichnov, K. Summerer, A. Ventura, J. P. Bondorf, A. S. Botvina, I. N. Mishustin, D. Boutin *et al.*, *Phys. Rev. C* **70**, 014902 (2004).
- [24] G. Antchev, P. Aspell, I. Atanasov, V. Avati, J. Baechler, V. Berardi, M. Berretti, E. Bossini *et al.*, *Europhys. Lett.* **96**, 21002 (2011).
- [25] M. Harrison, T. Ludlam, and S. Ozaki, *Nucl. Instrum. Methods A* **499**, 235 (2003).
- [26] W. Fischer, in *Proceedings of the International Particle Accelerator Conference 2010* (APAC, Kyoto, 2010), pp. 1227–1231.
- [27] J. G. Alessi, E. N. Beebe, S. Binello, C. J. Gardner, O. Gould, L. T. Hoff, N. A. Kling, R. F. Lambiase, V. LoDestro, R. Lockey, M. Mapes, A. McNerney, J. Morris, M. Okamura, A. Pendzick, D. Phillips, A. I. Pikin, D. Raparia, J. Ritter, T. C. Shrey, L. Smart, L. Snyderstrup, C. Theisen, M. Wilinski, A. Zaltsman, K. Zeno, U. Ratzinger, and A. Schempp, in *Proceedings of the Particle Accelerator Conference 2011* (IEEE, Piscataway, New Jersey, 2011), pp. 1966–1968.
- [28] V. Lebedev, in *Handbook of Accelerator Physics and Engineering*, 2nd ed., edited by A. W. Chao, K. H. Mess, M. Tigner, and F. Zimmermann (World Scientific, Singapore, 2013), pp. 155–159.
- [29] M. A. Furman and M. S. Zisman, in *Handbook of Accelerator Physics and Engineering*, 2nd ed., edited by A. W. Chao, K. H. Mess, M. Tigner, and F. Zimmermann (World Scientific, Singapore, 2013), pp. 311–318.
- [30] M. A. Furman, in *Proceedings of the Particle Accelerator Conference 1991* (IEEE, Piscataway, New Jersey, 1991), pp. 422–424.
- [31] C. Adler, A. Denisov, E. Garcia, M. Murray, H. Strobele, and S. White, *Nucl. Instrum. Methods A* **470**, 488 (2001).
- [32] Wenzel HF Ultra Low Noise OCXO, <http://www.wenzel.com/>.
- [33] A. Piwinski, in CERN Yellow Report 85-19-V2, 435, 1985 (unpublished).
- [34] N. V. Mokhov and V. I. Balbekov, in *Handbook of Accelerator Physics and Engineering*, 2nd ed., edited by A. W. Chao, K. H. Mess, M. Tigner, and F. Zimmermann (World Scientific, Singapore, 2013), pp. 269–271.
- [35] M. Syphers, in *Handbook of Accelerator Physics and Engineering*, 2nd ed., edited by A. W. Chao, K. H. Mess, M. Tigner, and F. Zimmermann (World Scientific, Singapore, 2013), pp. 360–362.
- [36] W. Fischer, M. Bai, and P. Harvey, BNL C-A/AP/235, 2006 (unpublished).

- [37] M. Seidel, DESY HERA 93-04, 1993 (unpublished).
- [38] M. Seidel, Ph.D. thesis, Hamburg University, DESY 94-103, 1994 (unpublished).
- [39] K.-H. Mess and M. Seidel, *Nucl. Instrum. Methods A* **351**, 279 (1994).
- [40] W. Fischer, M. Giovannozzi, and F. Schmidt, *Phys. Rev. E* **55**, 3507 (1997).
- [41] BERGOZ Instrumentation, 01170 Crozet, France, <http://www.bergoz.com>
- [42] K. Evans, <http://www.invasens.co.uk/FluxgateExplained.PDF>
- [43] K. B. Unser, *IEEE Trans. Nucl. Sci. NS* **16**, 934 (1969).
- [44] Keithley 220 Current Source, <http://www.keithley.com/products/searchresults?q=220&sa.x=29&sa.y=12>
- [45] Keithley 2000 DMM, <http://www.keithley.com/data?asset=359>
- [46] J. C. Denard, A. Saha, and G. Laveissiere, in *Proceedings of the Particle Accelerator Conference 2001* (IEEE, Piscataway, New Jersey, 1991), pp. 2326–2328.
- [47] M. Blaskiewicz (private communication).
- [48] J. Bergoz (private communication).
- [49] S. White, Ph.D. thesis, Université Paris-Sud 11, LAL-154, CERN-THESIS-2010-139 (2010) (unpublished).
- [50] A. Drees, BNL C-A/AP/495, BNL-103466-2013-IR, [arXiv:1312.6618](https://arxiv.org/abs/1312.6618) [physics.acc-ph].